Research Square

Preprints are preliminary reports that have not undergone peer review.
They should not be considered conclusive, used to inform clinical practice,
or referenced by the media as validated information.

Vertically aligned large area CVD grown MoS_2 nanoflakes based heterojunction for UV-Vis range photodetection: An electrical study

Pallavi Gupta
Jaypee Institute of Information Technology
SANDEEP CHHOKER
sandeep.chhoker@mail.jiit.ac.in

Jaypee Institute of Information Technology

Research Article

Keywords: Chemical vapour deposition, MoS2

Posted Date: September 15th, 2026

DOI: https://doi.org/10.21203/rs.3.rs-10186434/v1

License: This work is licensed under a Creative Commons Attribution 4.0 International License. Read Full License

Additional Declarations: No competing interests reported.

Version of Record: A version of this preprint was published at Journal of Materials Science: Materials in Electronics on October 15th, 2026. See the published version at https://doi.org/10.1007/s10854-026-18609-7.

Abstract

This study presents an Al/n-MoS_2/p-Si heterojunction photodetector, utilizing a large-area vertically aligned film synthesized via single-zone chemical vapor deposition. FE-SEM imaging confirms a uniform, vertically aligned flaky morphology with thin tip widths (10–20 nm), while Raman spectroscopy verifies highly coupled, crystalline multilayers.

Electrical evaluations from 100 kHz to 1 MHz up to a 10 V bias assess charge transport under dark, UV, and visible illumination. The IV characteristics show predominantly ohmic contact at the metal-semiconductor interface, ensuring efficient carrier injection. Under light, the device exhibits enhanced conduction: conductance rises by 14.8% under UV and 2.8% under visible illumination compared to dark conditions. The superior UV response stems from higher-density photogenerated carriers and electron accumulation at the vertical flakes' sharp tips. Finally, frequency-dependent CV and GV measurements reveal interface trap states that influence carrier dynamics, highlighting this heterojunction’s strong promise for photodetection

1. INTRODUCTION

Photodetectors (PDs), which transduce optical radiation into measurable electrical signals, represent indispensable building blocks in modern optoelectronic and photonic systems, encompassing digital imaging, optical communication, encompassing digital imaging, optical communication, environmental monitoring, and biomedical sensing. Their operational performance is typically quantified in term of responsivity (AW^{-1}), specific detectivity (Jones), quantum efficiency and photo gain which normalize for device geometry and noise characteristic to enable cross comparison across platforms. Two-dimensional (2D) transition metal dichalcogenides (TMDs) are a class of layered materials consisting of a transition metal atom layer (such as Mo or W) sandwiched between two chalcogen atom layers (S, Se, or Te). The individual layers are bonded together through weak van der Waals interactions, enabling their separation into monolayer and bilayer or few-layer nanosheets. These thin layers can be obtained using techniques such as mechanical exfoliation [1–6] and liquid-phase exfoliation[7] [8–10]. A 2D layer's atoms are structurally tightly connected by in-plane covalent or ionic forces, whereas adjacent layers are weakly coupled by vdW forces. [11, 12] This arrangement enables bulk crystal exfoliation into monolayers and simple integration on any substrate. Because of its distinctive structure, which offers mechanical flexibility, optical transparency, and high light matter interaction, 2D TMDs material is a viable option for flexible, conformal photodetectors of the future. [13] [14] Direct bandgap MoS_2 has attracted significant attention as a promising material for advanced optoelectronic applications. Owing to its atomically thin structure, tuneable electronic properties, and excellent chemical stability, MoS_2 often demonstrates advantages over graphene in devices requiring a direct bandgap. These distinctive characteristics make MoS_2 highly suitable for next-generation photodetectors, light-emitting diodes (LEDs), and photovoltaic devices. [15, 16] Bulk MoS_2 possesses an indirect bandgap of approximately 1.2 eV, however when thinned down to a monolayer it transforms into a direct bandgap semiconductor with a bandgap of about 1.8–1.9 eV (via K-K′ point matching). This transition is highly important for efficient light emission and strong light–matter interaction. In addition, MoS_2 exhibits a very high optical absorption coefficient (up to ~ 1.40×10^7 cm^{-1}) in the visible region (400–700 nm) making it a potential candidate for light harvesting applications.[17] MoS_2 based devices have also demonstrated excellent photoresponsivity, showing high sensitivity toward visible light, which can be further enhanced by integrating MoS_2 with other materials such as graphene, ZnO or $BaTiO_3$ to form hybrid heterostructures. Owing to its atomically thin structure and absence of dangling bonds, MoS_2 provides efficient

charge transport and fast carrier dynamics. Furthermore, it exhibits high mechanical flexibility and structural stability, making it suitable for flexible and wearable optoelectronic devices. [18]

In particular, MoS_2 -based photodetectors have reported high-performance sensing applications.[19] Both Bi_2Se_3 and GaS photodetectors exhibit comparatively less photodetection performance evaluated compared to MoS_2. While GaS photodetectors generally showed detectivity in the range of 4.39×10^{12} Jones, while GaS typically exhibits responsivity of 1–20 A/W and detectivity around 10^{10}-10^{11}Jones,[20] whereas high performance MoS_2 photodetectors can achieve responsivity ≥ 10^3A/W and detectivity ≥ 10^{13}Jones due to their superior light absorption and carrier transport. [21, 22]

Several strategies have been explored to further improve its performance such as heterostructure engineering by combining MoS_2 with other 2D materials such as WSe_2, SnS_2, or graphene to form type-II band alignment that enhances charge separation and improves device efficiency. Similarly, defect engineering through vacancy creation, doping (such as Cu, N doping). [23] or ion irradiation can modify the band structure and enhance optical absorption. Twist engineering in multilayer structures, such as controlling 2H and 3R stacking, has also been shown to significantly enhance photoresponsivity. [24]

Despite these advances, challenges still remain in improving overall photo-conversion efficiency and achieving a broader spectral response. However, the ability to tune the structural and electronic properties of MoS_2 continues to make it one of the most promising materials for next-generation flexible and high-performance optoelectronic devices, although some issues still need more better optimization. MoS_2 thin film can be synthesized by employing several techniques including mechanical exfoliation, hydrothermal method, sputtering and chemical vapour deposition (CVD). But mechanical exfoliation, hydrothermal method and sputtering etc have some limitation which inherently limited to small area, nonuniform coating over substrate[25], however hydrothermal provides a cost-effective route for large scale production, but they suffer from poor crystallinity and non-uniform morphology and uncontrolled layer thickness Sputtering, on the other hand, is compatible with industrial deposition systems but typically requires post-deposition annealing and careful parameter optimization to reduce defect density and improve film quality [26] Among these techniques, CVD is the most effective approach for synthesizing high-quality MoS_2 thin films. In particular, CVD enables wafer-scale and substrate-independent growth, where uniform monolayer or few-layer MoS_2 can be deposited over large areas (from centimetres-scale to full wafer-scale substrates) with excellent spatial continuity. This large-area growth is achieved through controlled vapor-phase transport of precursor species, uniform sulfurization kinetics, and optimized substrate–precursor interactions, which together promote homogeneous nucleation and lateral grain growth. As a result, continuous MoS_2 domains with reduced grain boundaries and improved crystallographic alignment can be obtained, which is critical for minimizing scattering centres and enhancing charge transport properties. Furthermore, CVD provides precise control over film thickness, layer number, and domain size by tuning growth parameters such as temperature, pressure, carrier gas flow rate, and precursor concentration. This level of control ensures high reproducibility and compatibility with standard semiconductor processing, making CVD highly suitable for scalable integration of MoS_2 into optoelectronic and nano electronic devices [27]. Unlike conventional planar MoS_2 films, vertically aligned MoS_2 exposes a larger density of active edge states, which facilitates enhanced photon absorption, carrier separation, and vertical transport pathways. Furthermore, illumination-dependent impedance and C-V/G-V studies on such heterojunctions remain comparatively unexplored

In this study, we focus on the CVD-based sulfurization of thermally deposited MoO_3 precursors to synthesize large area and vertically aligned multilayered MoS_2 thin films and their subsequent implementation in Al/n-MoS_2/p-Si

heterojunction photodetector. The structural and optoelectronic characteristics of the fabricated devices are systematically examined using Raman spectroscopy and FESEM complemented by detailed current–voltage (I–V), capacitance–voltage (C–V), and conductance–voltage (G–V) analyses under different illumination includes dark, UV and Visible illuminated conditions. This work aims to establish a direct correlation between sulfurization parameters, microstructural evolution, and device-level photodetection performance, providing valuable insight into optimizing growth conditions for high- responsivity, broadband, and stable n-MoS_2 based.

2. EXPERIMENTAL DETAILS:

2.1 Material and Reagents:

Molybdenum (VI) oxide from Sigma Aldrich, Sulphur from CDH were obtained while the Deionized water (DM-H2O) used obtained from Avarice, Isopropanol from CDH ethanol from Changshu Hor NA and acetone from Qualigens. They were used without any further purification and treatments

2.2 MoS_2 film synthesis:

Figure 1 shows a schematic diagram of the chemical vapor deposition (CVD) system used for the synthesis of MoS_2 thin films, where α-MoO_3 and Sulphur powder were used as precursor materials.

Figure 2 presents an inset view in which 0.5 g of α-MoO_3 and 1.5 g of Sulphur were placed in separate crucible positioned 22 cm apart inside the furnace chamber. The substrate was placed face down over the MoO_3 crucible. A continuous flow of argon gas was introduced for 20 minutes to establish an inert atmosphere. The pressure was maintained at 0.1 mbar, and the system was purged with argon gas at 0.5 mbar. The temperature was then increased to 600^{o}C over a period of 30 minutes, after which the crucible was held at this temperature for 40 minutes.

2.3 Device fabrication:

A device structure, comprising Al/n-MoS2/p-Si was assembled on a (111) oriented p-type Si (substrate). The substrate has a thickness of 280 μm and a specific resistivity ranging from 1–10 ohm-cm as shown in Fig. 2. Prior to deposition, the Si substrates underwent RCA cleaning, consisting of successive steps aimed at eliminating organic impurities, stripping the surface oxide, and removing ionic contaminants to ensure a pristine and defect-free surface. Following the RCA cleaning process, aluminium (Al) contacts of size 2 mm were fabricated on the silicon substrate using thermal evaporation under high vacuum environment with the pressure of 2 x 10^{-6} Torr. This method provided a uniform metal layer with good interfacial adhesion, ensuring stable electrical contact for subsequent device characterization.

2.4 Experimental Details:

The structural analysis of the samples was done using Raman spectroscopy at an excitation wavelength of 514 nm by Raman Spectrometer (Horiba Jobin Yvon). The morphology study of p-Si/n-MoS2 was assessed by the FESEM respectively (FEI NOVA NANOSEM450). The I-V, C-V-F and G-V-F measurement of the vertical device were carried out using Keysight B2901B SMU. All these measurements were conducted under room temperature and in Dark, visible light (550 nm) and UV light (365 nm) at 100 kHz – 1 MHz

3. Result and Discussion:

3.1 Structural Studies

Raman Spectroscopy

Figure 3 shows the Raman spectrum of the synthesized n- MoS_2 layer recorded using a 514 nm laser excitation source. Two prominent first-order Raman peaks, characteristic of hexagonal MoS_2, are clearly observed. These peaks correspond to the in-plane E^1_{2g}vibrational mode at 384 cm^{-1} and the out-of-plane A_{1g}vibrational mode at 408.7 cm^{-1}. [28, 29] The presence of these distinct zone-centre phonon modes confirms the crystalline quality of the synthesized material. The frequency difference between the two Raman modes, defined as $\Delta = A_{1g} - E^1_{2g}$, is widely recognized as an important parameter for determining the thickness and number of layers in n-MoS_2. In the work, the measured separation of 24.8 cm^{-1} suggests the formation of multilayer n-MoS_2, which agrees well with previously reported studies on CVD-grown MoS_2 films. [30] [2] Previously reported studies generally observed that with an increase in the number of layers, the E^1_{2g} mode shifts toward lower frequency, whereas the A_{1g}mode shifts toward higher frequency. The increase in layer thickness enhances the interlayer van der Waals interactions, which restrict atomic vibrations and increase the effective force constant. As a result, both vibrational modes are theoretically expected to stiffen, leading to a blue shift. The experimentally observed blue shift of the A_{1g}mode with increasing layer number is therefore in good agreement with this prediction. However, unlike the A_{1g} mode, the E^1_{2g} mode exhibits a red shift rather than a blue shift. Importantly, the observed Raman peak separation (~ 24.8 cm^{-1}) suggests multilayer MoS_2 with strong interlayer coupling. This behaviour indicates that the influence of interlayer van- der Waals forces on this mode is relatively weak. Instead, structural modifications induced by stacking and long-range Coulombic interlayer interactions in multilayer MoS_2 are likely to play a dominant role in altering the atomic vibrational behaviour. [28, 31]. Additionally, the relatively sharp Raman peaks indicate good crystallinity and low phonon scattering. The vertically aligned morphology may further contribute to phonon confinement near edge planes, where local lattice asymmetry and unsaturated sulphur bonds modify the vibrational environment. Since vertically standing nanoflakes expose a large density of edge sites, localized strain and defect-induced phonon softening may also contribute to minor peak broadening.

Morphological Analysis

FESEM Studies

The surface morphology of the MoS_2 layer deposited on the p-Si substrate was investigated using FE-SEM, as shown in Fig. 4(a and b), at magnifications of 40,000× and 150,000×, respectively. Figure 4(a) reveals the large-area growth of MoS_2 nanoflakes synthesized by chemical vapor deposition (CVD) on the p-Si substrate. The magnified FE-SEM image in Fig. 4(b) clearly demonstrates that the as-grown MoS_2 nanoflakes are nearly perpendicular to the p-Si (100) substrate surface, indicating the formation of vertically aligned structures. [32, 33] The growth initially begins with the formation of nanoscale spike like particles, which subsequently develop into densely packed and uniformly distributed MoS_2 nanoflakes randomly oriented across the substrate. The nanoflakes possess lengths in the range of 220–240 nm, while the vertically aligned n-MoS_2 exhibit tip diameter in the range of 10–20 nm. The possible discussion for vertical alignment in thermal CVD is as follows- The formation of vertically aligned MoS_2 nanoflakes during sulfurization is governed by anisotropic growth kinetics and surface energy minimization during the CVD process. Initially, sulphur vapor reacts with thermally evaporated MoO_3 to form intermediate suboxide species

$MoO_3 + xS \; MoO_{3-x} + SO_2$……a)

In general, in a CVD, at the early stage of growth, lateral nucleation dominates due to lower surface diffusion barriers. As the sulphur concentration and local strain increase, the basal planes become energetically unstable for further horizontal expansion. Consequently, vertical edge-oriented growth becomes thermodynamically favourable. Some conditions that help initiate vertical alignment in thermal CVDs are; excess sulphur promotes rapid edge growth rates compared to basal plane growth; as the film thickness increases, accumulated strain energy at the MoS_2/substrate interface suppresses planar growth and induces vertical flake formation; the exposed edge planes possess higher surface energy and chemical activity, leading to anisotropic crystal growth along the c-axis direction and at moderate growth temperature (~ 600°C), surface diffusion length becomes insufficient for large lateral grain coalescence, promoting vertically oriented nanoflakes. It is pointed that; vertical alignment of active material is crucial for photodetection as edge sites provide enhanced optical absorption wherein carrier extraction paths become shorter and out-of-plane transport resistance also decreases at 10–20 nm length scale.

At this length scale, carrier transport begins to experience spatial restriction, leading to the emergence of size depended electronic effects. Although the characteristic dimensions remain larger than the exciton radius of n-MoS_2, the system approaches a regime where weak quantum confinement effect may begin to contribute. In previous studies, such confinement in nanoscale semiconductor is typically associated with a changing of the band structure (E_g), where the bandgaps tend to increase as the spatial dimension decrease due to the discretization of energy levels and reduce dielectric screening. [34] In this report, the reduce tip dimension may therefore induce slight bandgap widening compared to bulk MoS_2, although the effect is exposed to be weak in magnitude rather than quantum dot. Although the nanospike dimensions are not sufficiently small for strong quantum confinement, reduced lateral dimensions and edge-dominated morphology may induce localized electronic modification. Furthermore, the vertically aligned n-MoS_2 nanoflakes expose a large number of edge sites facing upward, resulting in a high density of active surface sites and enhanced charge transport characteristics [35]. It is worth pointing that 15–20 layers (~ 10–15 nm) MoS_2 behaves as a quasi-direct band gap material especially when there are sufficient doping states available at the surface. In this study, the vertical alignment of nanoflakes is a feature of sulphur doping and thus the possible quasi-direct band transition (K-Ḱ points are ~ 1.3–1.4 eV apart) under external bias has initiated in MoS_2 nanoflakes.

Further, layered materials generally exhibit significantly higher in-plane conductivity than out-of-plane conductivity due to weak van der Waals interactions between adjacent layers, the vertically standing structure of n-MoS_2 provides direct pathways for carrier transport from the junction interface to the top Al electrode.[36] The vertically oriented nanoflakes shorten the carrier transport distance and facilitate rapid movement of photogenerated electrons and holes along the vertical direction, thereby minimizing carrier recombination losses. In addition, the exposed edge planes and enlarged interlayer spacing enhance photon absorption and promote efficient charge separation at the n-MoS_2/p-Si heterojunction. The continuous vertical pathways also improve carrier mobility and electrical connectivity between the active layer and the electrode, leading to faster carrier extraction and improved photo response performance.[37] Therefore, the unique vertically aligned MoS_2 nanospike morphology is highly beneficial for optoelectronic and photodetector applications requiring efficient carrier transport and high photo sensitivity.

Electrical Studies

1. **Dark, Visible & UV Illumination I-V Characteristic of Al/ $\varvec{n}-\varvec{M}\varvec{o}\varvec{S}_2$ /p-Si**

The Current-Voltage (I-V) characteristic of an electrical device represent a set of analytical curves used to investigate and evaluate its charge transport and conduction behaviour under varying applied bias condition which

demonstrates the link between the transporting current and the applied voltage. I-V characteristic curves are employed to find and study the primary device parameter with the aid of mathematical methods that describe its transporting process. Figures (5a) shows the photo response of a synthesized Al/n-MoS_2/p-Si device under dark Visible light illumination ($\lambda = 550\ nm$) and UV illumination ($\lambda = 365\ nm$) at 300K (room temperature). Under all measurements, its demonstrated good ohmic transport between the synthesized n-MoS_2 over p-Si Substrate and Aluminium electrode with linear curve.

The ohmic behaviour of the photodetector demonstrate the low resistance and non-rectifying connection between the semiconductor and the electrodes. The observed ohmic response can be correlated with the energy band diagram Fig. 6 of the n-MoS_2/p-Si interface. The large density of edge sites observed in the FE-SEM facilitates efficient charge carrier transport across the heterointerface by promoting favourable band alignment and reducing the effective barrier height for electron and hole injection. Unlike Schottky based photodetectors, ohmic contact devices usually operates as photoconductor. This indicate that their current-voltage (I-V) relationship is symmetric and linear. I-V results of device showed a positive response, as we expected. The electrical conductance of the sample was extracted from the slope of the linear current-voltage (I-V) characteristics in accordance with Ohm's Law, were conductance

$$\varvec{G} = \frac{dI}{dV}$$

1

The measured conductance in dark was found to be 1.42 × $10^{-4}\ S$. Upon illumination with Visible light, the conductance increased slightly to 1.46 × $10^{-4}\ S$, corresponding to an enhancement of approximately 2.8% and Under ultraviolet (UV) illumination, the conductance increased slightly to 1.63 × $10^{-4}\ S$, was observed and corresponding to an enhancement of approximately 14.8% as compare to dark. This increase in conductance with the illumination intensity and photon energy indicate photoconductive behavior of the device (Al/n-MoS_2/p-Si). Similar results were reported by Abhay V. Agrawal et al. [38] in their study on UV-assisted NO_2 gas sensing, where UV illumination significantly enhanced the sensing sensitivity and accelerated the recovery behaviour due to improved charge carrier generation and interfacial charge transport.

Figure 5b illustrates the logarithmic I–V characteristics of the device, showing a junction centered at zero bias that produces a symmetric response, which is beneficial for photodetector applications. When operated at low bias voltages, the photocurrent is typically weak, and the dark current becomes the dominant contribution to the total current. Under these conditions, important performance metrics such as responsivity, sensitivity and noise level can be extracted from the I–V behavior.

The symmetry of the curve indicates that the device can function effectively under both forward and reverse bias and the nature of the junction observed in the log I–V plot provides information about the device's noise characteristics. A sharp and well-defined junction suggests low noise performance, where as a broadened or distorted junction indicates the higher noise levels [39]. Further, the linearity of the I–V curves suggests dominant ohmic transport at low bias, whereas slight deviations at higher bias may indicate trap-assisted carrier transport across interface defect states. Performance metric of the photodetector, such as responsivity, specific detectivity and sensitivity are calculated by using the following equations.[40]. Responsivity reflects how effectively the device converts incident light into an electrical signal, and is defined as the ratio of photocurrent to the power of the incoming light. Specific detectivity represents the detector's ability to identify weak signals in the presence of noise,

normalized with respect to its active area and bandwidth. Sensitivity, on the other hand, is expressed as the ratio of photocurrent to dark current, indicating how well the detector distinguishes signal from background current.

$$R = \frac{I_{ph}}{pA}$$

2

$$D^* = \frac{A^{\frac{1}{2}}}{(2eI_{dark}{}^2)}$$

3

$$S = \frac{I_{ph}}{I_{dark}}$$

4

Where, I_{ph} = $I_{Visible/UV}$ – I_{dark} where $I_{Visible/UV}$ and I_{dark} are the photocurrent and the dark current, p represent the UV & Visible source power density; A denotes detector's active area, and e is the elementary charge ($1.602 \times 10^{-19} C$). These parameters were calculated and tabulated in Table 1. It is pointed that, the enhanced UV response originates from the larger photon energy of UV radiation, which exceeds the effective transition energy more efficiently and generates a higher density of electron–hole pairs. Additionally, vertically aligned edge-rich MoS_2 structures possess abundant unsaturated bonds that contribute to enhanced UV absorption and carrier transport.

Table 1
Photo-response parameter of Al/n-MoS2/p-Si

Illumination	Responsivity	Photosensitivity	Detectivity
	mA/W	(+ ve)	(Jones)
UV	320	0.077	2.78×10^{9}
Visible	80	0.019	7.0×10^{8}

1. **Dark, Visible & UV Illumination C-V-F Characteristic of Al/ $\varvec{n} - \varvec{M}\varvec{o}\varvec{S}_2$ /p-Si**

Figure 7 (a-c) represented the capacitance-voltage characteristics measured at different frequencies from 100 kHz to 1 MHz under visible, UV and dark illumination. In all cases, the capacitance exhibits a pronounced peak around –1V, followed by as frequency increase, the capacitance gradually decrease is consistent with the model proposed by Nicollian and Goetzbergern which attributes the phenomenon to the response of interface states that can follow the alternating signal at lower frequencies. At lower frequencies, the total measured capacitance reflects the combined contribution of the space charge region and interface state capacitance. As the frequency increase, lead to the limited response of interface states and charge carrier, which are unable to response the applied AC signal thereby reducing their influence on total capacitance. Illuminations (Dark, visible & UV) significantly influences the C–V response. Under Dark condition (Fig. 5c) exhibits the lowest capacitance values, reflecting the absence of photo-generated carriers and the dominance of intrinsic material properties.

Under visible light (Fig. 7a), the capacitance increases compared to the dark condition, indicating the generation of additional charge carriers. This effect becomes more pronounced under UV illumination (Fig. 7b), where the capacitance reaches its maximum values across all frequencies. The enhanced response under UV exposure is attributed to the higher photon energy, which promotes more efficient generation of electron–hole pairs, leading to increased charge accumulation and polarization within the device. Under dark condition (Fig. 7c) exhibits the lowest capacitance values, reflecting the absence of photo-generated carriers and the dominance of intrinsic material properties. Overall, the results demonstrate that both frequency and illumination play critical roles in modulating the electrical behaviour of the device, with UV illumination and low-frequency operation yielding the highest capacitance response.

Figure 8. (a, b and c) is A^2/C^2 – V characteristic of the Al/n-MoS_2/p-Si yield a straight line, where A is the area of the contacts used analysed to extract electrical parameters such as donor concentration (N), built-in potential (V_{bi}), and depletion width (W_d). The Al top contact had a diameter of 1 mm, corresponding to an effective device area (A) of 0.00785 cm^2. The dielectric constant of silicon (ε_s) was taken as $11.7\varepsilon_o$, where $\varepsilon_o = 8.854 \times 10^{-14}$ F/cm, and the effective density of states in the valence band (N_v) was assumed to be 1.04×10^{19} cm^{-3}. In the Al/n-MoS_2/p-Si structure depletion layer capacitance is expressed as, based on the 1 MHz. [41, 42]

$$\frac{A^2}{C^2} = \frac{2(V_{bi} + V - \frac{KT}{q})}{N_D \epsilon_s}$$

5

Where/, V: applied Voltage of the device; q: magnitude of the electric charge and V_{bi} determine by extrapolating the $1/C^2$ -V curve on the voltage axis.

The semiconductor Donar density (N_D) is obtained by slop of the A^2/C^2-V and the resultant calculated value is

$$N_D = \frac{2}{q\epsilon_s \times \ Slope}$$

6

Based on the parameters extracted from the C–V-F plot, the Built-in potential of the device in all cases were evaluated using the standard relation.

$$\phi_B = V_{bi} + \frac{KT}{q} \ln \left[\frac{N_V}{N_D} \right]$$

7

The depletion width (W) corresponding to a particular reverse bias voltage (V) was calculated from the measured capacitance value using the standards relation.

$$W = \sqrt{\frac{2\epsilon_s (V_{bi} + V)}{qN_D}}$$

8

These values are concluded in the Table 2.

Only a marginal reduction in depletion width (from 115 to 112 nm) under illumination was observed, suggesting moderate photocarrier-induced modulation of the junction electric field. It is worthy to point out that the reason for marginal reduction in depletion region could be that the device still operates in partially depleted regime, interface traps limit complete carrier separation or recombination processes suppress strong depletion collapse. Thus, illumination mainly modifies interfacial charge distribution rather than drastically altering the junction structure.

Table 2
The values of donor concentration, built-in Potential Vbi and Width of of Al/ $\varvec{n} - \varvec{M}\varvec{o}\varvec{S}_2$/p-Si

Illumination	Nd(cm^{-3})	Vbi (V)	W_d (nm)
Dark	1.22×10^{17}	0.254	115
Visible	1.21×10^{17}	0.247	114
UV	1.29×10^{17}	0.246	112

The capacitance-Voltage(C-V) characteristics of the p-Si/n-MoS_2/Al structure were investigated over a wide frequency range from 100 kHz to 1000kHz in order to analyses the interface properties of the device. Both C-V and G-V (conductance-voltage) measurement clearly indicates that the capacitance and conductance are strongly influenced by the applied bias voltage as well as the measurement frequency. The variation give rise to well defined regions i.e. accumulation, depletion, and inversion, each corresponding to different biasing conditions as depicted in Fig. 9 [43]

For negative bias voltages, the device operates in the inversion region, where the capacitance remains relatively constant and shows minimal dependence on the applied voltage. As the voltage increases toward moderate values, the device transitions into the depletion region, followed by the accumulation region at higher positive voltages. In this regime, both capacitance and conductance begin to increase significantly due to the enhanced presence of charge carriers at the interface. At lower frequencies, the C–V curves exhibit a noticeable peak, which is attributed to the contribution of interface states. These states are capable of responding to the applied AC signal depending on their relaxation time (τ), thereby increasing the measured capacitance. In contrast, at higher frequencies, the interface states are unable to follow the rapid AC signal, and a different type of peak appears in the accumulation region. This high-frequency peak is mainly associated with the effect of series resistance within the device, which alters the overall capacitance response. [39, 44, 45].

The frequency-dependent C–V characteristics indicate that carrier transport in the Al/n-MoS_2/p-Si heterojunction is strongly influenced by interface states and trap-assisted charge dynamics. At low frequencies (100–200 kHz), interface trap states can effectively follow the applied AC signal. Therefore, the measured capacitance includes contributions from depletion capacitance, interface state capacitance and minority carrier response. As frequency increases toward 1 MHz, interface states fail to respond to the rapidly oscillating AC field because their

Table 3
Comparison table for MoS_2/Si based PDs

Structure Type	Fabrication Route	Spectral Range	Bias Voltage	Responsivity	Detectivity	Remarks	Ref.
Planar MoS_2/Si PD	Mechanically exfoliated MoS_2 on Si	Visible	5 V	~ 20–200 mA/W	~ 10^9–10^{10} Jones	Moderate carrier transport due to planar geometry	[11], [21]
Planar CVD MoS_2/Si PD	CVD-grown planar MoS_2 film	UV–Visible	1–10 V	~ 0.1–1 A/W	~ 10^{10}–10^{11} Jones	Large-area growth with improved uniformity	[13], [25], [27]
Vertical MoS_2/Si PD	CVD-grown vertically aligned nanosheets	UV–NIR	Self-powered to 5 V	~ 1–10 A/W	~ 10^{11}–10^{12} Jones	Fast carrier extraction and reduced recombination	[32], [33], [35]
MoS_2/GaN Vertical PD	Vertical MoS_2 on GaN nanorods	UV	3–5 V	~ 2–15 A/W	~ 10^{12} Jones	Strong UV selectivity with enhanced edge transport	[37]
Bi_2Se_3/Si PD	Thermal evaporation heterostructure	Broadband	3–10 V	~ 0.5–2 A/W	~ 10^{10}–10^{11} Jones	Broadband photo response	[20], [22]
TiO_2/NiO UV PD	Hydrothermal heterostructure	UV	Self-powered	~ 100–300 mA/W	~ 10^{10} Jones	Low dark current and improved charge separation	[40]
Present Work: Vertical Al/n-MoS_2/p-Si PD	Sulfurized CVD-grown vertically aligned MoS_2 nanoflakes	UV–Visible	10 V	320 mA/W (UV)	2.78 × 10^9 Jones	Edge-rich morphology with illumination-dependent C–V/G–V analysis	This work

emission/capture time constants exceed the signal period and thus capacitance decreases. The capacitance peak near negative bias indicates strong trap-assisted polarization and carrier accumulation at the MoS_2/Si interface. The observed dispersion behavior confirms significant interface state density, non-ideal type II heterojunction behavior and frequency-dependent relaxation processes.

1. **G-V-F Characteristic of Al/ $\varvec{n} - \varvec{M}\varvec{o}\varvec{S}_2$ /p-Si Dark, Visible & UV Illumination**

Figure 10 (a,b and c) demonstrates the conductance–voltage (G–V) characteristics of the device measured over a frequency range from 100 kHz to 1 MHz under Visible, UV and dark illumination. The conductance response is found to be highly sensitive in both the accumulation and depletion regions, where noticeable variations occur with changing frequency. However, at higher frequencies, the conductance becomes nearly independent of both the applied bias voltage and frequency, indicating the limited ability of charge carriers to respond to the applied AC

signal. This behaviour is mainly attributed to the presence of electronic interface states within the forbidden energy band gap. These states originate from interface imperfections such as dangling bonds, surface states, and periodic lattice disorder present at the semiconductor/metal interface.[41]. The interface states play an important role in determining the electrical behaviour of the device by trapping and releasing charge carriers, thereby influencing the charge exchange and recombination mechanisms at the interface. Consequently, both the capacitance–voltage (C–V) and conductance–voltage (G–V) characteristics are strongly affected by the density, distribution, and dynamic response of these interface states. [46]

Conclusion:

In this work, a vertically aligned Al/n-MoS_2/p-Si heterojunction photodetector was successfully fabricated using CVD-grown multilayer MoS_2 nanoflakes and systematically investigated for UV–Visible photodetection applications. Raman spectroscopy confirmed the successful formation of crystalline multilayer MoS_2 for strong interlayer coupling and layered growth. FESEM analysis revealed densely distributed vertically aligned MoS_2 nanoflakes with lateral dimensions of approximately 220–240 nm and tip widths of nearly 10–20 nm. The edge-rich vertically standing morphology provides enhanced active surface area, improved light absorption, and efficient vertical carrier transport pathways, which are highly beneficial for optoelectronic applications. The electrical characterization exhibited nearly linear and symmetric I–V characteristics under dark, visible, and UV illumination conditions, indicating quasi-ohmic transport behaviour and efficient charge injection across the heterointerface. The enhanced photocurrent under UV illumination is due to higher photon energy and increased photogenerated carrier density, along with efficient carrier extraction due to the presence of vertically aligned edge-oriented MoS_2 nanoflakes. The device exhibited responsivities of 320 mA/W and 80 mA/W under UV and visible illumination, respectively, demonstrating superior response toward UV radiation. Frequency-dependent C–V measurements performed in the range of 100 kHz to 1 MHz revealed strong illumination- and frequency-dependent interfacial charge dynamics. The reduction in built-in potential from 0.254 V under dark conditions to 0.246 V under UV illumination, accompanied by a slight decrease in depletion width from 115 nm to 112 nm, indicates photocarrier-induced modulation of the junction electric field. The observed capacitance dispersion at lower frequencies suggests significant contribution from interface trap states, which can follow the AC signal due to their finite relaxation times. At higher frequencies, these interface states become unable to respond to the rapidly varying signal, resulting in reduced capacitive contribution. Furthermore, G–V analysis confirmed the presence of interface states associated with dangling bonds, structural imperfections, and localized surface defects at the MoS_2/Si interface. These interface states strongly influence carrier trapping, recombination, and relaxation mechanisms, thereby governing the transport characteristics and overall photodetection performance of the device. Overall, the vertically aligned Al/n-MoS_2/p-Si heterostructure demonstrates promising UV–Visible photodetection capability owing to its edge-rich morphology, efficient vertical charge transport, and illumination-modulated interfacial electrical properties.

Declarations

Conflict of interest

the author declare that they have no conflict of interest.

Ethical approval

The manuscript is prepared according to the ethical standard of the journal.

Consent to participate:

Not applicable

Consent to publication:

The authors have given consent for publication as per the journal policy.

Funding:

Not applicable.

Author Contribution

Pallavi Gupta: Data curation, Formal analysis, Investigation, Methodology, Writing: original draft. Sandeep Chhoker: Conceptualization, Formal analysis, Supervision, Validation, Writing – review & editing.

Acknowledgement

VLSI Lab JIIT

Data Availability

All data supporting the findings of this study are available within the paper in form of plots and figues. If required data will be provided.

Code availability:

Not applicable.

References

1. K.S. Novoselov, D. Jiang, F. Schedin, T.J. Booth, V.V. Khotkevich, S.V. Morozov, A.K. Geim, (2005). Two-dimensional atomic crystals., Two-dimensional atomic crystals, Proc. Natl. Acad. Sci. U.S.A. 102, 10451–10453 (2005)
2. H. Li, Z. Yin, Q. He, H. Li, X. Huang, G. Lu, D.W.H. Fam, A.I.Y. Tok, Q. Zhang, H. Zhang, Fabrication of single- and multilayer MoS_2 film-based field-effect transistors for sensing NO at room temperature. Small. **8**, 63–67 (2012)
3. O. Lopez-Sanchez, D. Lembke, M. Kayci, A. Radenovic, A. Kis, Ultrasensitive photodetectors based on monolayer MoS_2. Nat. Nanotechnol. **8**, 497–501 (2013). 10.1038/nnano.2013.100

4. B. Radisavljevic, A. Radenovic, J. Brivio, V. Giacometti, A. Kis, Single-layer MoS_2 transistors. Nat. Nanotechnol. **6**, 147–150 (2011). 10.1038/nnano.2010.279
5. Z. Yin, H. Li, H. Li, L. Jiang, Y. Shi, Y. Sun, G. Lu, Q. Zhang, X. Chen, H. Zhang, Single-layer MoS_2 phototransistors. ACS Nano. **6**, 74–80 (2012). 10.1021/nn2024557
6. A. Splendiani, L. Sun, Y. Zhang, T. Li, J. Kim, C.-Y. Chim, G. Galli, F. Wang, Emerging photoluminescence in monolayer MoS_2. Nano Lett. **10**, 1271–1275 (2010)
7. A. Jawaid, D. Nepal, K. Park, M. Jespersen, A. Qualley, P. Mirau, L.F. Drummy, R.A. Vaia, Mechanism for liquid phase exfoliation of MoS_2. Chem. Mater. **28**, 337–348 (2016)
8. K. Funaki, K. Tezuka, Y. Shan, Liquid-phase exfoliation of ultrathin layered transition metal dichalcogenide nanosheets composed of solid-solution $Mo_{1-x}W_xS_2$. Phys. Status Solidi A **211**, 901–904 (2014)
9. D.B. Velusamy, R.H. Kim, S. Cha, J. Huh, R. Khazaeinezhad, S.H. Kassani, G. Song, S.M. Cho, S.H. Cho, I. Hwang, J. Lee, K. Oh, H. Choi, C. Park, Flexible transition metal dichalcogenide nanosheets for band-selective photodetection. Nat. Commun. **6**(1), 8063 (2015)
10. J.N. Coleman, M. Lotya, A. O'Neill, S.D. Bergin, P.J. King, U. Khan, K. Young, A. Gaucher, S. De, R.J. Smith, I.V. Shvets, S.K. Arora, G. Stanton, H.-Y. Kim, K. Lee, G.T. Kim, G.S. Duesberg, T. Hallam, J.J. Boland, J.J. Wang, J.F. Donegan, J.C. Grunlan, G. Moriarty, A. Shmeliov, R.J. Nicholls, J.M. Perkins, E.M. Grieveson, K. Theuwissen, D.W. McComb, P.D. Nellist, V. Nicolosi, Two-dimensional nanosheets produced by liquid exfoliation of layered materials. Science. **331**, 568–571 (2011)
11. W. Choi, M.Y. Cho, A. Konar, J.H. Lee, G.-B. Cha, S.C. Hong, S. Kim, J. Kim, D. Jena, J. Joo, S. Kim, High-detectivity multilayer MoS_2 phototransistors with spectral response from ultraviolet to infrared. Adv. Mater. **24**, 5832–5836 (2012)
12. K.F. Mak, C. Lee, J. Hone, J. Shan, T.F. Heinz, Atomically thin MoS_2: A new direct-gap semiconductor. Phys. Rev. Lett. **105**, 136805 (2010)
13. W. Zhang, J.-K. Huang, C.-H. Chen, Y.-H. Chang, Y.-J. Cheng, L.-J. Li, High-gain phototransistors based on a CVD MoS_2 monolayer. Adv. Mater. **25**, 3456–3461 (2013)
14. F. Strauß, C. Schedel, M. Scheele, Edge contacts accelerate the response of MoS_2 photodetectors. Nanoscale Adv. **5**, 3494–3499 (2023)
15. B.K. Bareth, M. Khan, A. Tripathi, M.N. Tripathi, Ion-irradiation induced structural, electronic, and optical properties modification in a few layered MoS_2. Nucl. Instrum. Methods Phys. Res. Sect. B **554**, 165436 (2024)
16. M. Timpel, G. Ligorio, A. Ghiami, L. Gavioli, E. Cavaliere, A. Chiappini, F. Rossi, L. Pasquali, F. Gärisch, E.J.W. List-Kratochvil, P. Nozar, A. Quaranta, R. Verucchi, and M. V. Nardi, 2D-MoS_2 goes 3D: Transferring optoelectronic properties of 2D MoS_2 to a large-area thin film, *npj 2D Mater. Appl.* 5, 64 (2021)
17. O. Samy, S. Zeng, M.D. Birowosuto, A. El, Moutaouakil, A review on MoS_2 properties, synthesis, sensing applications and challenges. Crystals. **11**, 355 (2021)
18. S. Swann, Magnetron sputtering. Phys. Technol. **19**, 67–75 (1988)
19. W. Pan, A. Wang, X. Wu, X. Zheng, H. Chen, S. Qin, Z.V. Han, S. Zhao, R. Zhang, F. Wang, A fast 2D MoS_2 photodetector with ultralow contact resistance. Nanoscale. **16**, 21061–21067 (2024)
20. H. Zhang, X. Zhang, C. Liu, S.-T. Lee, J. Jie, High-responsivity, high-detectivity, ultrafast topological insulator Bi_2Se_3/silicon heterostructure broadband photodetectors. ACS Nano. **10**, 5113–5122 (2016)
21. P. Han, E.R. Adler, Y. Liu, L. St Marie, A. El Fatimy, S. Melis, E. Van Keuren, P. Barbara, Ambient effects on photogating in MoS_2 photodetectors. Nanotechnology. **30**, 284004 (2019)

22. X. Hong, J. Shen, X. Tang, Y. Xie, M. Su, G. Tai, J. Yao, Y. Fu, J. Ji, X. Liu, J. Yang, D. Wei, High-performance broadband photodetector with in-situ-grown Bi_2Se_3 film on micropyramidal Si substrate. Opt. Mater. **117**, 111118 (2021)
23. N. Thomas, S. Mathew, K.M. Nair, K. O'Dowd, P. Forouzandeh, A. Goswami, G. McGranaghan, S.C. Pillai, 2D MoS_2: Structure, mechanisms, and photocatalytic applications. Mater. Today Sustain. **13**, 100073 (2021)
24. R.M.A. Khalil, F. Hussain, A.M. Rana, M. Imran, G. Murtaza, Comparative study of polytype 2H-MoS_2 and 3R-MoS_2 systems by employing DFT. Phys. E. **106**, 338–345 (2019)
25. J. Jeon, S.K. Jang, S.M. Jeon, G. Yoo, Y.H. Jang, J.-H. Park, S. Lee, Layer-controlled CVD growth of large-area two-dimensional MoS_2 films. Nanoscale. **7**, 1688–1695 (2015)
26. R. Garg, S. Gonuguntla, S. Sk, M.S. Iqbal, A.O. Dada, U. Pal, M. Ahmadipour, Sputtering thin films: Materials, applications, challenges and future directions. Adv. Colloid Interface Sci. **330**, 103203 (2024)
27. C. Lee, H. Yan, L.E. Brus, T.F. Heinz, J. Hone, S. Ryu, Anomalous lattice vibrations of single- and few-layer MoS_2. ACS Nano. **4**, 2695–2700 (2010)
28. B. Chakraborty, H.S.S.R. Matte, A.K. Sood, C.N.R. Rao, Layer-dependent resonant Raman scattering of a few-layer MoS_2. J. Raman Spectrosc. **44**, 92–96 (2013)
29. X. Zhang, W.P. Han, J.B. Wu, S. Milana, Y. Lu, Q.Q. Li, A.C. Ferrari, P.H. Tan, Raman spectroscopy of shear and layer breathing modes in multilayer MoS_2. Phys. Rev. B **87**, 115413 (2013)
30. H. Li, Q. Zhang, C.C.R. Yap, B.K. Tay, T.H.T. Edwin, A. Olivier, D. Baillargeat, From bulk to monolayer MoS_2: Evolution of Raman scattering. Adv. Funct. Mater. **22**, 1385–1390 (2012)
31. L. Wang, J. Jie, Z. Shao, Q. Zhang, X. Zhang, Y. Wang, Z. Sun, S.-T. Lee, MoS_2/Si heterojunction with vertically standing layered structure for ultrafast, high-detectivity, self-driven visible–near infrared photodetectors. Adv. Funct. Mater. **25**, 2910–2919 (2015)
32. Y. Zhang, Y. Yu, L. Mi, H. Wang, Z. Zhu, Q. Wu, Y. Zhang, Y. Jiang, In situ fabrication of vertical multilayered MoS_2/Si homotype heterojunction for high-speed visible–near-infrared photodetectors, *Small* 12, 1062–1071 (2016)
33. S. Abdullah, S. Hussain, M. Liaquat, Exploring quantum-confinement effects in two-dimensional materials synthesized via chemical vapor deposition for next-generation optoelectronic devices. Dialogue Social Sci. Rev. (DSSR). **3**, 167–185 (2025)
34. G.H. Shin, J. Park, K.J. Lee, G.-B. Lee, H.B. Jeon, Y.-K. Choi, K. Yu, S.-Y. Choi, Si–MoS_2 vertical heterojunction for a photodetector with high responsivity and low noise equivalent power. ACS Appl. Mater. Interfaces. **11**, 7626–7634 (2019)
35. H. Li, H. Wu, S. Yuan, H. Qian, Synthesis and characterization of vertically standing MoS_2 nanosheets. Sci. Rep. **6**, 21171 (2016)
36. G. Yang, Y. Gu, P. Yan, J. Wang, J. Xue, X. Zhang, N. Lu, G. Chen, Chemical vapor deposition growth of vertical MoS_2 nanosheets on p-GaN nanorods for photodetector application. ACS Appl. Mater. Interfaces. **11**, 8453–8460 (2019)
37. A.V. Agrawal, R. Kumar, S. Venkatesan, A. Zakhidov, G. Yang, J. Bao, M. Kumar, M. Kumar, Photoactivated mixed in-plane and edge-enriched p-type MoS_2 flake-based NO_2 sensor working at room temperature. ACS Sens. **3**, 998–1004 (2018)
38. K. Arjun, B. Karthikeyan, MoS_2/PEDOT:PSS nanocomposite films for deep UV sensing: Role of the radiation-induced trapping and localization of charges. Appl. Phys. A **129**, 543 (2023)

39. Y. Gao, J. Xu, S. Shi, H. Dong, Y. Cheng, C. Wei, X. Zhang, S. Yin, L. Li, TiO_2 nanorod arrays based self-powered UV photodetector: Heterojunction with NiO nanoflakes and enhanced UV photoresponse. ACS Appl. Mater. Interfaces. **10**, 11269–11279 (2018)
40. N. Kavasoglu, C. Tozlu, O. Pakma, A.S. Kavasoglu, S. Ozden, B. Metin, O. Birgi, S. Oktik, Room-temperature interface state analysis of Au/poly(4-vinyl phenol)/p-Si structure. Synth. Met. **159**, 1880–1884 (2009)
41. T. Wang, S. Peng, Z. Jin, C. Hu, H. Tian, Interface characterization of graphene–silicon heterojunction using Hg probe capacitance–voltage measurement. Adv. Mater. Interfaces. **11**, 2400184 (2024)
42. O. Pakma, N. Serin, T. Serin, Ş. Altındal, Influence of frequency and bias voltage on dielectric properties and electrical conductivity of Al/TiO_2/p-Si/p^+ (MOS) structures. J. Phys. D: Appl. Phys. **41**, 215103 (2008)
43. A. Mutlu, C. Tozlu, Electrical characterization of Ag/$MoO_{3-\square}$/p-Si Schottky diodes based on $MoO_{3-\square}$ synthesized via sol–gel method: An investigation on frequency and voltage dependence. J. Mater. Sci. : Mater. Electron. **35**, 805 (2024)
44. Ö. Berkün, M. Ulusoy, Ş. Altındal, B. Avar, On frequency and voltage dependent physical characteristics and interface states characterization of the metal semiconductor (MS) structures with (Ti:DLC) interlayer. Phys. B **666**, 415099 (2023)
45. C. Tozlu, A. Mutlu, Poly(melamine-co-formaldehyde) methylated effect on the interface states of metal/polymer/p-Si Schottky barrier diode. Synth. Met. **211**, 99–106 (2016)

Figures

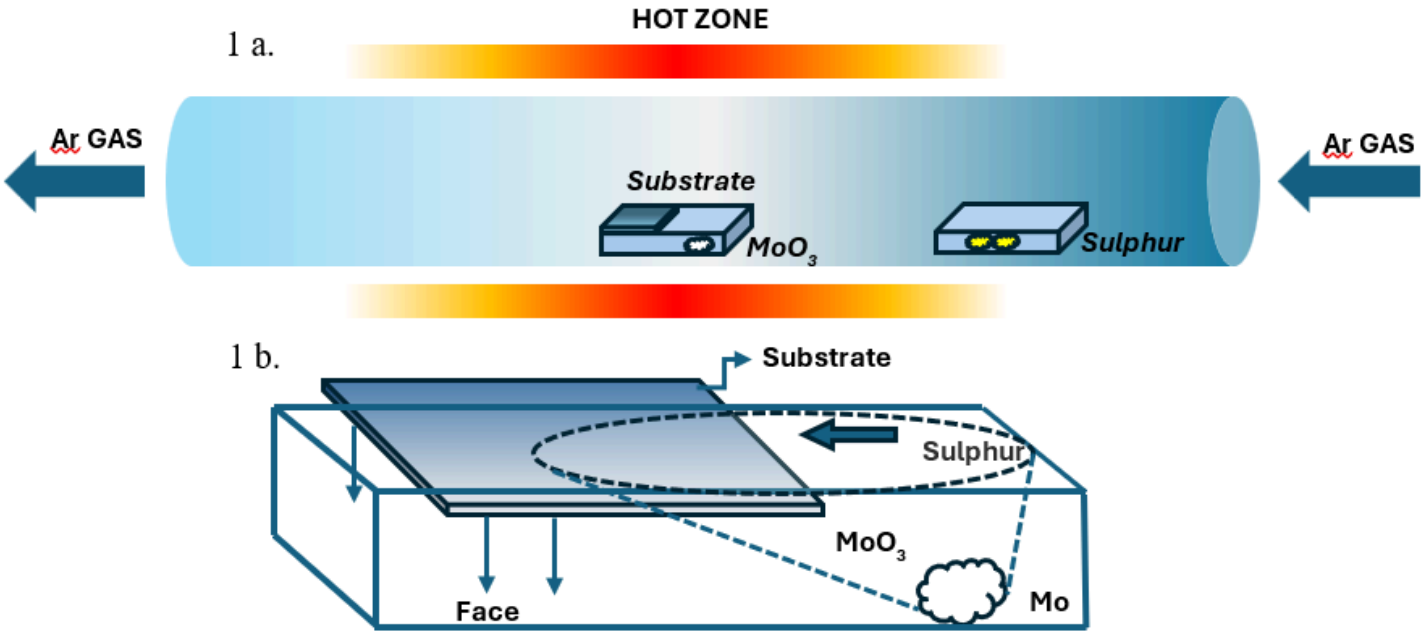


Figure 1

a. shows a schematic diagram of the chemical vapour deposition (CVD) system used for the synthesis of MoS_2 thin films, where MoO_3 and sulphur powder were used as precursor materials. **b.** Inset view of a Substrate in which 0.5 g of MoO3 and 1.5 g of sulphur were placed in separate crucibles positioned 22 cm apart inside the furnace chamber.

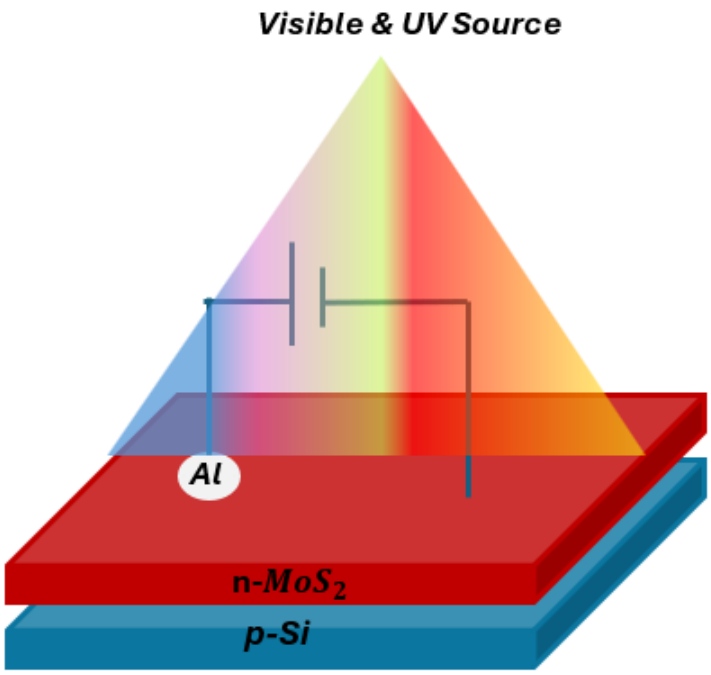


Figure 2

Systematic diagram of as synthesised ohmic device Al/n-MoS_2/p-Si.

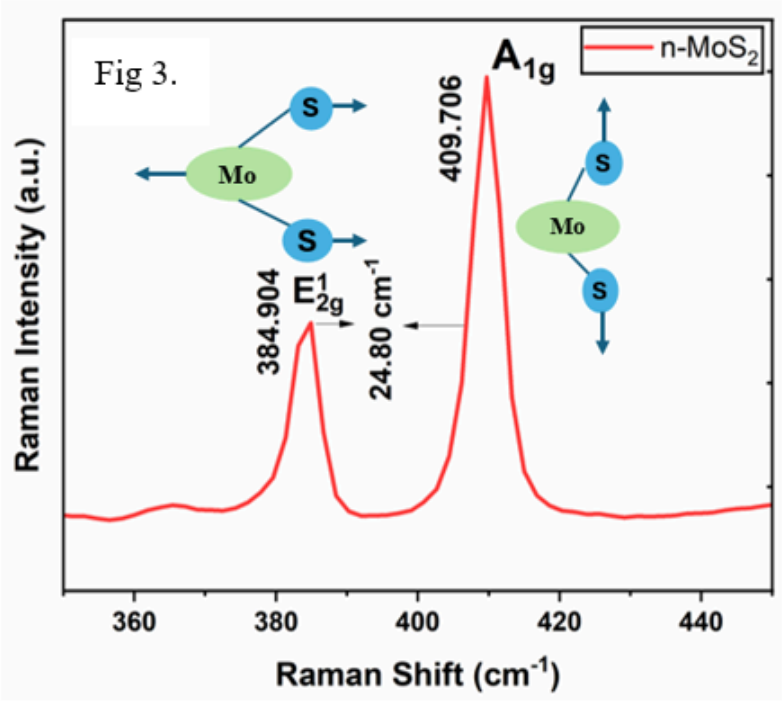


Fig 3. Raman spectrum and surface morphology of synthesized MoS2 thin film. Raman spectrum showing the characteristic Type equation here. and A_{1g} vibrational mode of MoS_2 confirming its formation

Figure 3

See image above for figure legend.

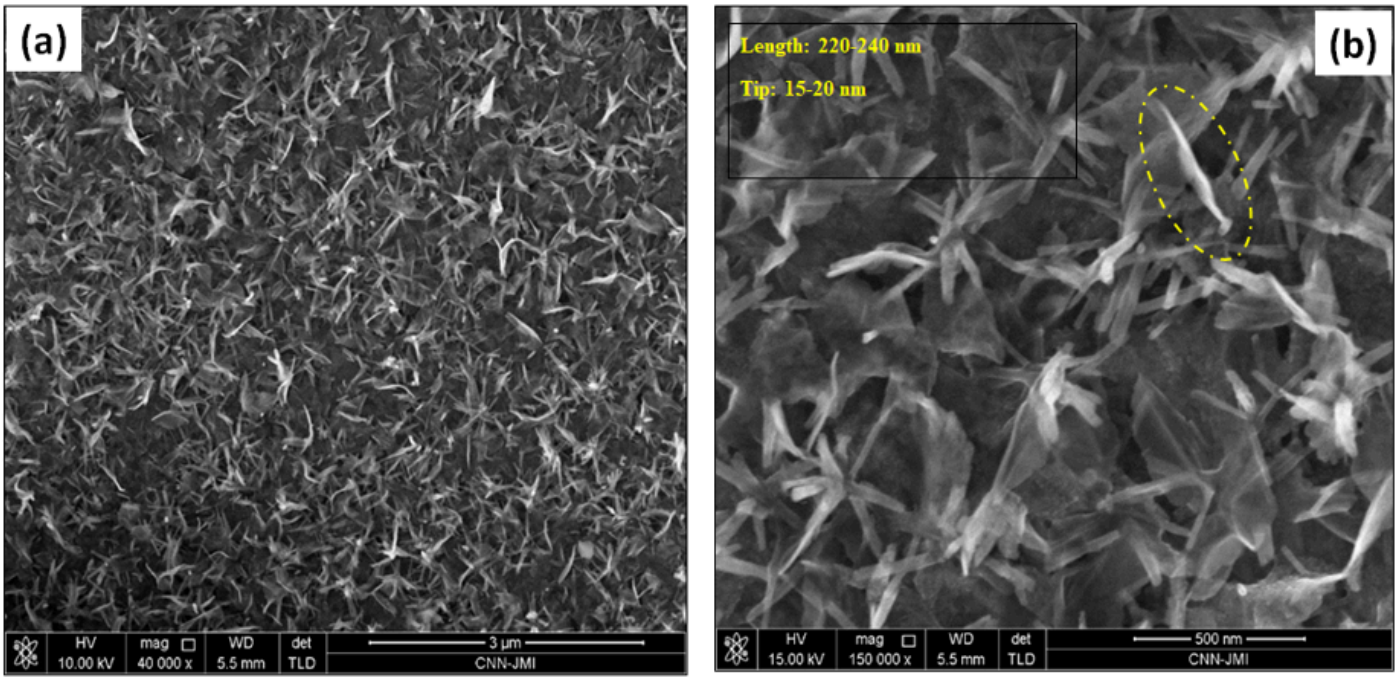


Fig. 4 a and b. Electrical microscopy image displaying the nanostructured morphology of the film at different magnification

Figure 4

See image above for figure legend.

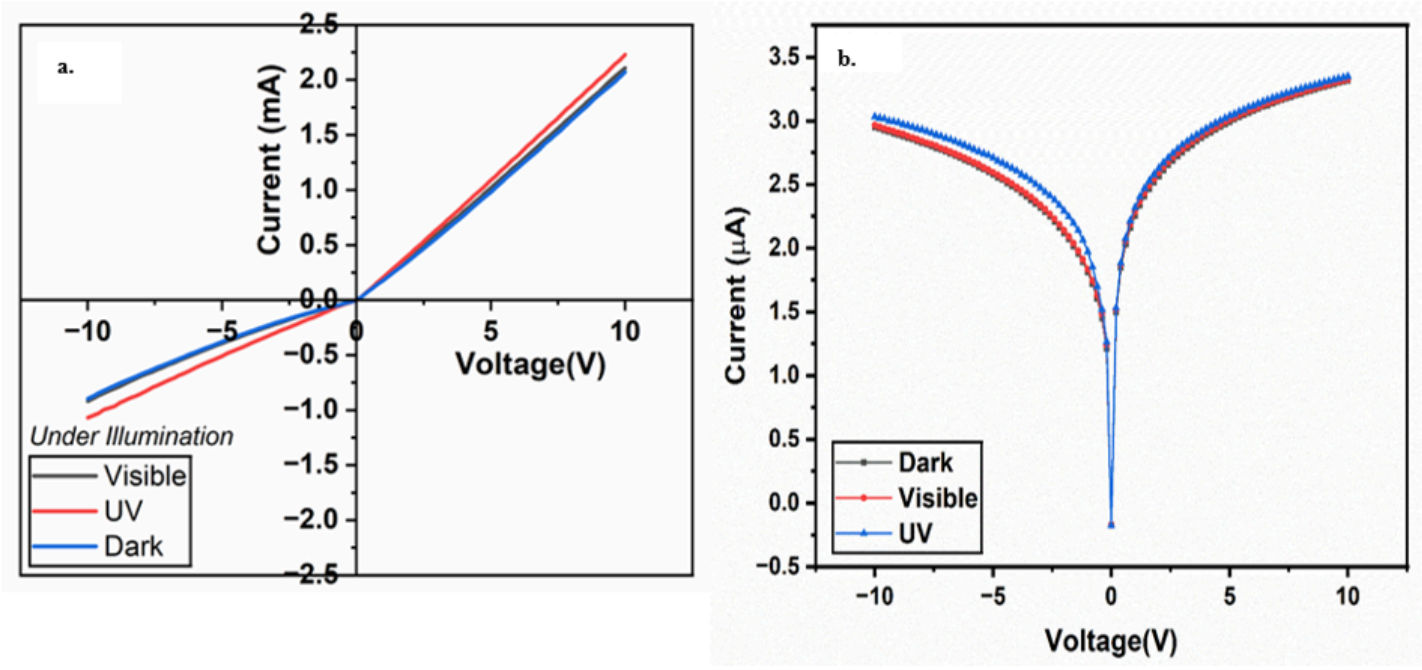


Fig.5 a. Current-Voltage (I-V) Characteristic under Visible, UV and Dark, **b.** Logarithmic plot of Current-Voltage Characteristic under Dark, Visible and UV of Al/n-MoS_2/p-Si.

Figure 5

See image above for figure legend.

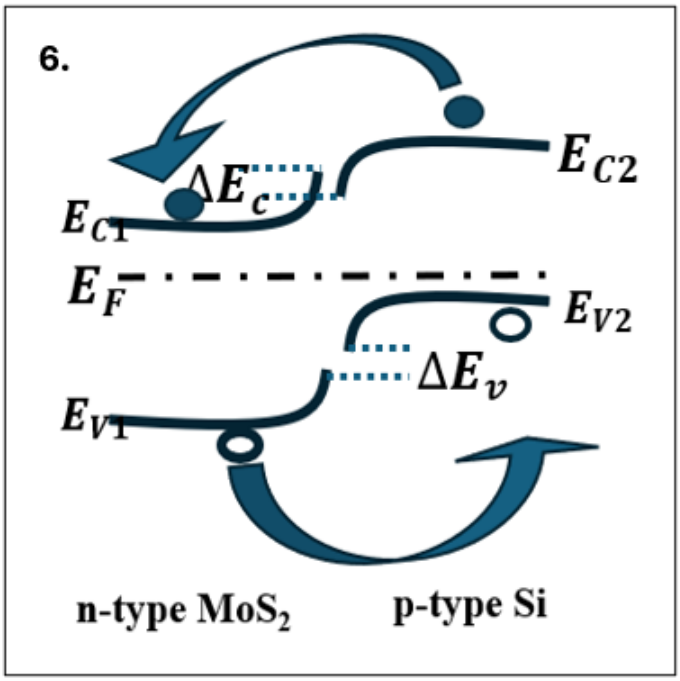


Figure 6

Energy band diagram of MoS_2/p-Si heterojunction.

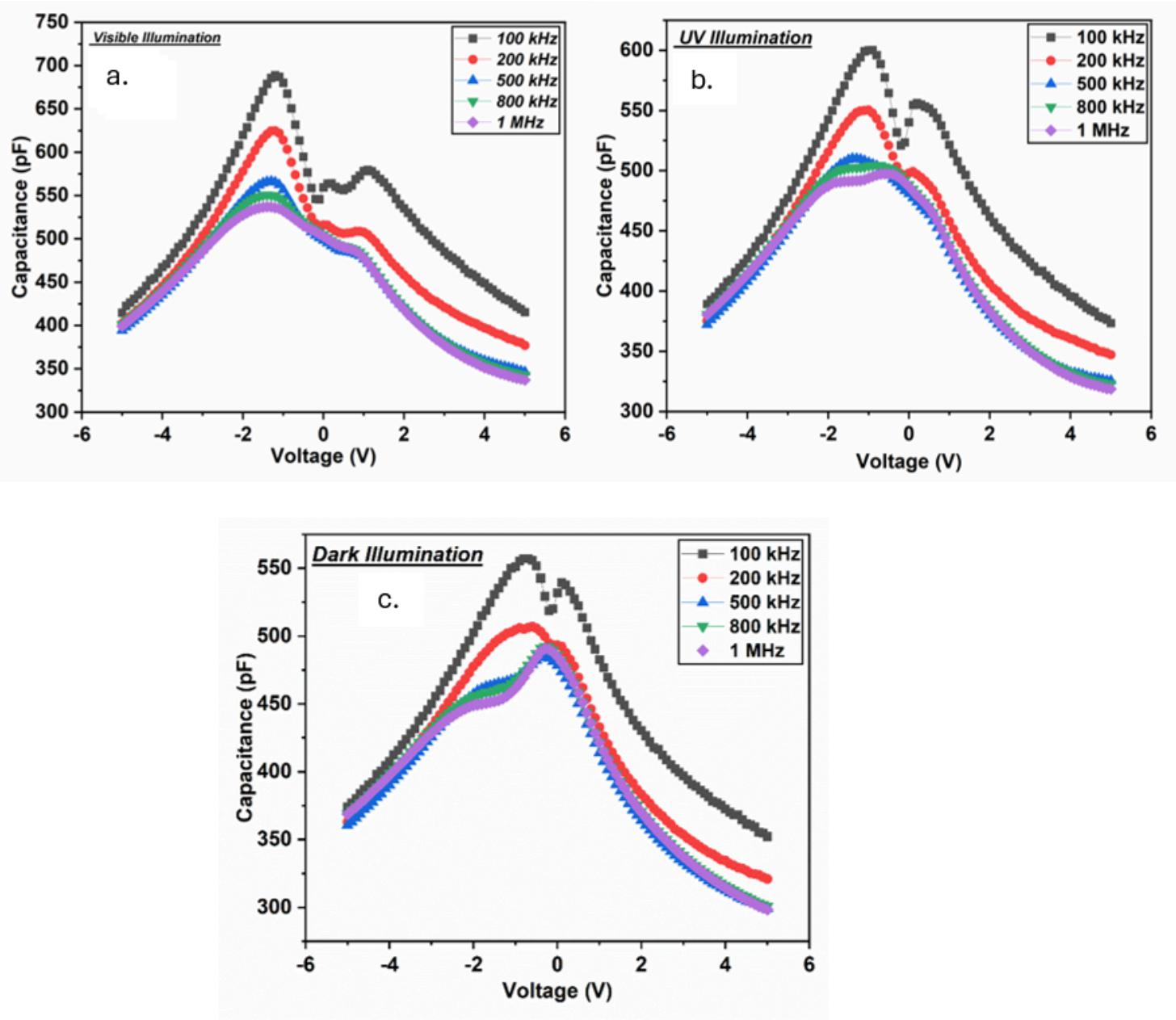


Figure 7

Capacitance-Voltage- Frequency (C-V-F) Characteristic under **a.** Visible, **b.** UV and **c.** Dark illumination

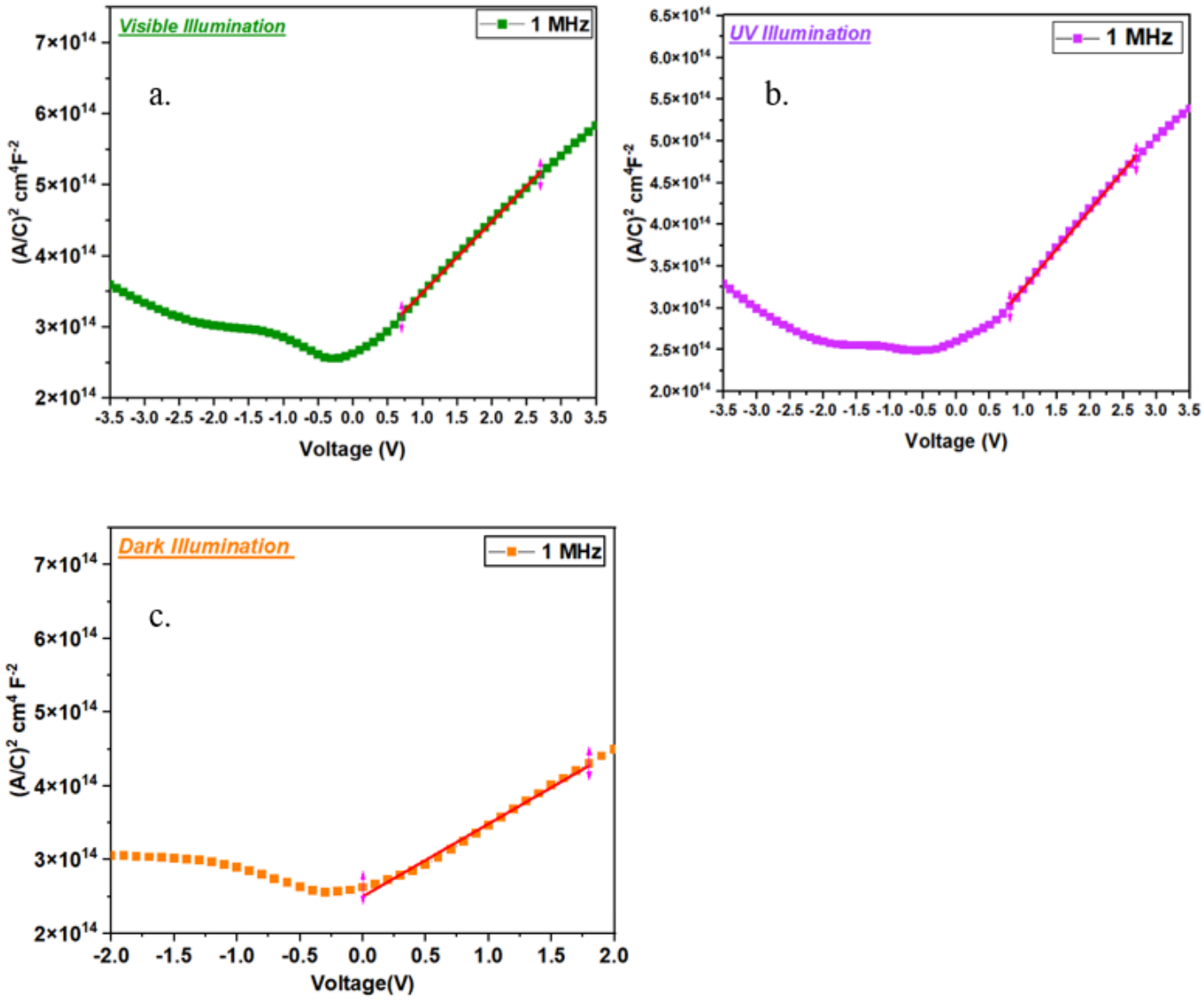


Figure 8

$(A/C)^2$-V at 1 MHz of Al/n-MoS2/p-Si under **a.** Visible **b.** UV **c.** Dark illumination

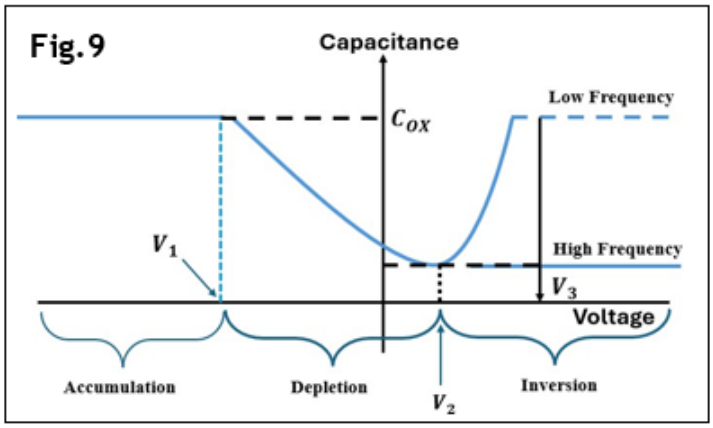


Figure 9

Capacitance-Voltage (C-V) characteristic showing accumulation, depletion and inversion regions, with distinctions between low frequency and high frequency Reponses

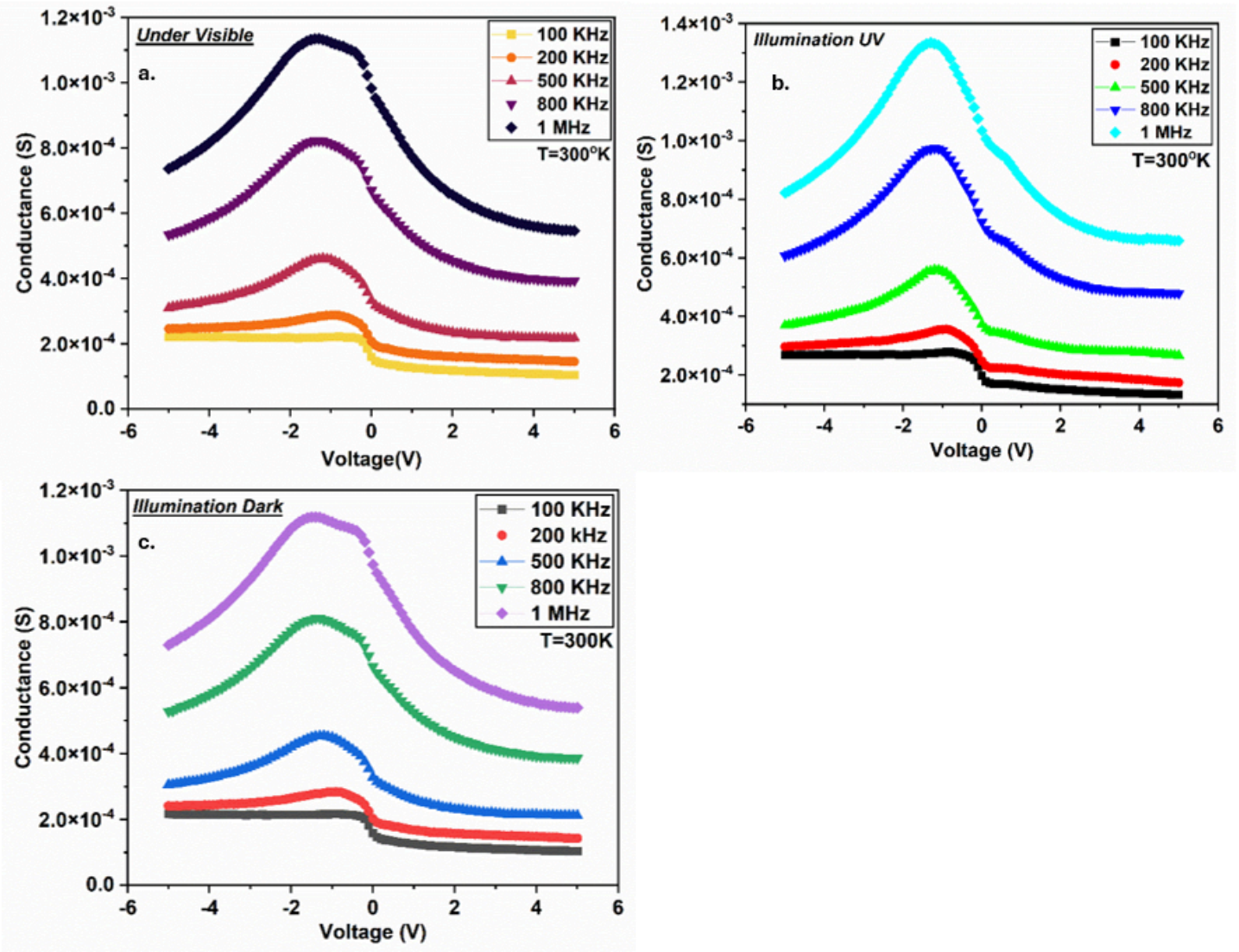


Figure 10

Conductance-Voltage- Frequency (C-V-F) Characteristic under **a.** Visible, **b.** UV and **c.** Dark illumination